Proceedings of Machine Learning Research vol 331:1–12, 2026 8th Annual Conference on Learning for Dynamics and Control

Realistic Internal Dynamics Are Essential for Human-Like Control: An Optimal Feedback Control Perspective

Nima Akbari NA994@NAU.EDU
Reza Sharif Razavian REZA.SHARIF-RAZAVIAN@NAU.EDU
Department of Mechanical Engineering, Steve Sanghi College of Engineering, Northern Arizona University, Flagstaff, Arizona, United States

Editors: G. Sukhatme, L. Lindemann, S. Tu, A. Wierman, N. Atanasov

Abstract

Humans skillfully control objects with internal dynamics, such as a bag of groceries that swings or a cup of coffee; yet the neural control principles underlying such dexterous coordination are not fully understood. An important question that remains to be answered is: How complex are humans' internalized representations of such systems (also known as the *internal models*)? This question has been tackled before using various model-based control architectures; however, the answers within the context of the leading neural control theory—the stochastic optimal feedback control (OFC)—remain elusive. To shed more light on this question, we ran OFC simulations of transporting an underactuated cart-pendulum system with varying levels of internal model detail and compared the results with human experimental data of the same task. Using OFC as the controller, our results showed that the internal model that matched the full dynamics of the cart-and-pendulum system reproduced human data most closely. These results are in contrast to a previous study that used *input shaping* as the control structure and concluded that a simplified internal model led to the most human-like behavior. In particular, when our internal model lacked impedance or coupling, the characteristic double-peak velocity profile did not emerge in simulation. But the full-detail internal model reproduced the characteristic two-peak velocity profile and maintained peak ratios consistent with experimental data, unlike simplified internal models, which produced substantially larger ratios. These results indicate that realistic internal dynamics and feedback structure are essential for capturing human-like manipulation, providing a blueprint for control policies and training of dexterous robots.

Keywords: Optimal feedback control, human movement, internal models, stochastic control, coupled object manipulation

1. Introduction

A central goal in computational neuroscience and motor control is to understand how the nervous system regulates movement in uncertain, dynamically changing environments. Humans manipulate tools and objects with internal dynamics despite delays, noise, and nonlinear body mechanics (Scott, 2004; Diedrichsen and Shadmehr, 2023). A prevalent view is that the brain relies on internal models of body and environment dynamics within closed-loop control architectures to make predictions, compensate for noise and delays, and plan optimal actions (Wolpert et al., 2011; Franklin and Wolpert, 2011).

The stochastic Optimal feedback control theory (commonly known as the OFC) provides a normative account of such control behavior: Given a dynamical internal model, noise statistics, and task objective, the control policy minimizes an expected cost of accuracy,

effort, and stability (Todorov and Jordan, 2002; Todorov, 2004). OFC-based models explain features of point-to-point reaching, flexible feedback gains, and task-dependent variability (Scott, 2004; Huang et al., 2011; Harris and Wolpert, 1998; Lizarraga and Shadmehr, 2023). In parallel, extensive evidence supports adaptive internal models that map motor commands to sensory consequences and capture environmental dynamics (Shadmehr and Krakauer, 2010; Wolpert et al., 2011; Lillicrap and Scott, 2013).

How detailed these internal representations must be remains an open question. Interacting with complex objects and environments provides a stringent test. Bazzi et al. (2023) showed that humans controlling a cup-and-ball system (equivalent to a cart-and-pendulum) exhibit a characteristic double-peaked velocity profile and stable internal dynamics (Figure 1b). Using an input-shaping—a deterministic, feed-forward, model-based control structure—they argued that human behavior can be captured most accurately by using a simplified internal model: one that omits the underactuated dynamics of the cart-and-pendulum but includes the arm's linear impedance. While intriguing, it remains unclear as to whether Bazzi et al. 's conclusions hold when considering the feedback and stochastic structure of the neural control system.

We address this question by directly comparing human data from Bazzi et al. (2023) with OFC simulations of the same mechanical system. We construct an OFC controller for a cart-pendulum-impedance model with fixed physical parameters, process and sensory noise, and terminal stabilization costs, and evaluate its predictions without participant-specific tuning. We then introduce mismatched internal models (no coupling of internal dynamics, no impedance) to test which representations are compatible with the experimental data. By quantifying discrepancies via root-mean-square error (RMSE), normalized errors, and a velocity peak ratio metric, we evaluate how far a principled OFC framework with realistic internal dynamics can account for human control of complex objects.

2. Experimental Task and Data

We used the experimental data from Bazzi et al. (2023), where participants used a robotic manipulandum to control a virtual cup-and-ball system (Figure. 1a). The task involved transporting the cup to a target location along a straight line while avoiding loss of the ball during transport and minimizing its residual oscillations at the target. Only the two final experimental blocks (blocks 3 and 4, after familiarization blocks) were considered here. Participants were instructed to arrive at the target in 1.40 s and 1.20 s, in blocks 3 and 4, respectively. Figure 1b shows representative hand-velocity trajectories for a participant exhibiting a double-peak velocity profile. For visualization, the trajectories were temporally cropped to emphasize the movement phase, where the dominant velocity peaks occur.

3. OFC Model and Simulation Framework

3.1. Dynamical model of the task

We consider a one-dimensional cart-and-pendulum system as a mechanical analog of carrying a cup with an internal mass (Figure. 2a). We used the same approach to model this system as prior work (Sharif Razavian et al., 2023). In this model (Figure. 2b), cart position x represents the hand/cup motion; the pendulum, with angle ϕ, captures internal dynamics

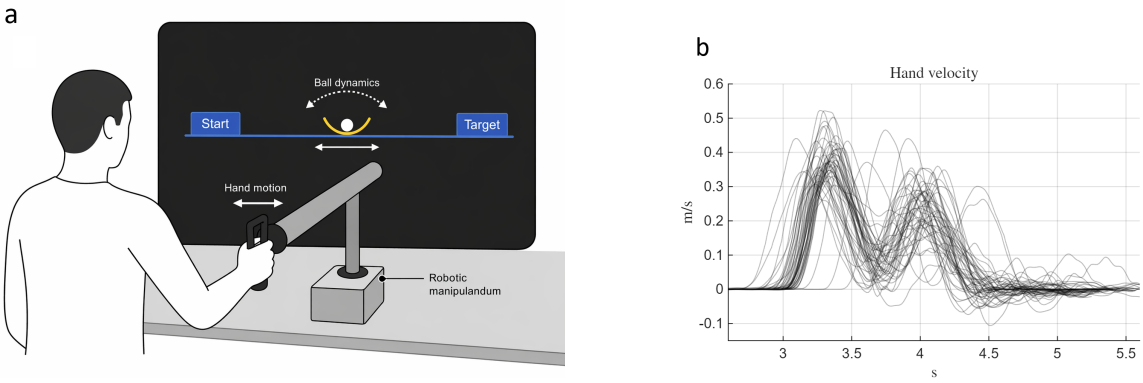

Figure 1: (a) The experimental setup from (Bazzi et al., 2023). Participants interacted with a virtual cup-and-ball system through a robotic manipulandum. Horizontal hand motion controlled the cup position, while ball dynamics (pendulum) were displayed on a screen. The task was to transport the ball while minimizing its final oscillations. (b) Experimental hand velocity trajectories for participant S1 (Block 3), showing trial-to-trial variability and double-peak velocity profiles.

that must be stabilized. A muscle-driven reference mass M_{ref} is connected via stiffness k_h and damping b_h to a hand/cart (with masses M_{arm} and M, respectively), which is coupled to the pendulum's mass m at a distance l. The coupled system is modeled by the following continuous-time equations, linearized around ($\phi \approx 0$):

$$(M_{\text{arm}} + M + m)\,\ddot{x} = -ml\,\ddot{\phi} + k_h(x_{\text{ref}} - x) + b_h(\dot{x}_{\text{ref}} - \dot{x}), \tag{1}$$

$$l\,\ddot{\phi} = -g\,\phi - G\,\ddot{x}, \tag{2}$$

$$\tau\,\dot{F} = u - F, \tag{3}$$

$$M_{\text{ref}}\,\ddot{x}_{\text{ref}} = k_h(x - x_{\text{ref}}) + b_h(\dot{x} - \dot{x}_{\text{ref}}) + F \tag{4}$$

Here, x_{ref} is the position of the reference mass, defining the pre-impedance trajectory, which is driven by the muscle force F, which in turn, is driven by the neural command u with a time constant τ. We use fixed parameters from prior studies (Bazzi et al., 2023; Sharif Razavian et al., 2023): M=1.9 kg, m=1.1 kg, M_{arm}=0.5 kg, M_{ref}=0.5 kg, l=0.5 m, g=9.81 m/s^2, k_h=50 N/m, b_h=8 N s/m, τ=0.03 s. The term G is the coupling term between the cart acceleration and pendulum dynamics (typical value $G = 1$).

3.2. State-space formulation

We use a seven-dimensional state vector:

$$\mathbf{x} = \begin{bmatrix} x & \dot{x} & \phi & \dot{\phi} & x_{\text{ref}} & \dot{x}_{\text{ref}} & F \end{bmatrix}^{\mathsf{T}}, \tag{5}$$

to convert (1)–(4), to state-space form:

$$\dot{\mathbf{x}} = A\mathbf{x} + Bu + \boldsymbol{\xi} + \mathbf{n} \tag{6}$$

where

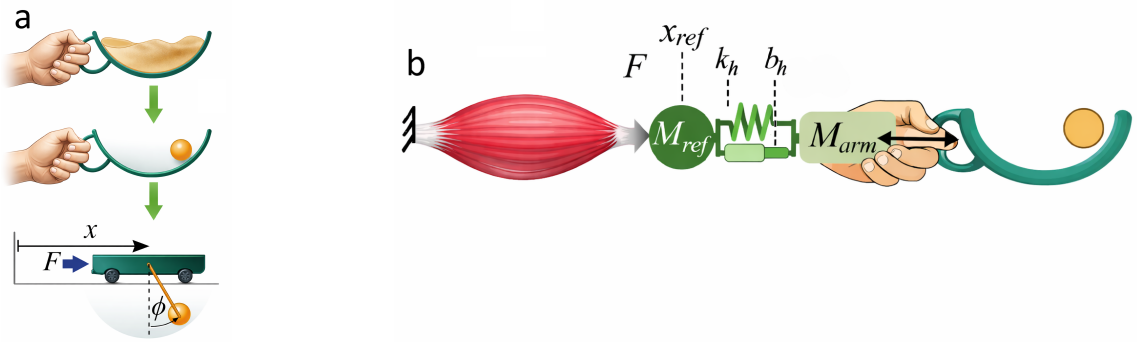

Figure 2: (a) Cup-and-ball interactions, inspired by the task of carrying a cup of coffee, are mechanically equivalent to a cart-and-pendulum. (b) Modeling the human control of the cup-and-ball system. Muscle-driven reference mass is coupled via impedance to arm/cart mass to control the object.

$$A = \begin{bmatrix} 0 & 1 & 0 & 0 & 0 & 0 & 0 \\ -\frac{k_h}{\alpha} & -\frac{b_h}{\alpha} & \frac{mg}{\alpha} & 0 & \frac{k_h}{\alpha} & \frac{b_h}{\alpha} & 0 \\ 0 & 0 & 0 & 1 & 0 & 0 & 0 \\ \frac{Gk_h}{l\alpha} & \frac{Gb_h}{l\alpha} & -\left(\frac{g}{l}+\frac{Gmg}{l\alpha}\right) & 0 & -\frac{Gk_h}{l\alpha} & -\frac{Gb_h}{l\alpha} & 0 \\ 0 & 0 & 0 & 0 & 0 & 1 & 0 \\ \frac{k_h}{M_{\text{ref}}} & \frac{b_h}{M_{\text{ref}}} & 0 & 0 & -\frac{k_h}{M_{\text{ref}}} & -\frac{b_h}{M_{\text{ref}}} & \frac{1}{M_{\text{ref}}} \\ 0 & 0 & 0 & 0 & 0 & 0 & -\frac{1}{\tau} \end{bmatrix}, \qquad B = \begin{bmatrix} 0 \\ 0 \\ 0 \\ 0 \\ 0 \\ 0 \\ \frac{1}{\tau} \end{bmatrix} \tag{7}$$

and $\alpha = M_{\text{arm}} + M + m - mG$. Here $\boldsymbol{\xi} \sim \mathcal{N}(0, \Omega_\xi)$ represents additive process noise and $\mathbf{n}$ is multiplicative control-dependent (signal-dependent, Harris and Wolpert (1998)) noise:

$$\mathbf{n} = \epsilon\, C\, u, \tag{8}$$

where $\epsilon \sim \mathcal{N}(0, 1)$ and C is noise scaling matrix.

For use in the OFC framework, the continuous-time system (6) is discretized with a sampling interval $\Delta t = 0.01\,\text{s}$:

$$\mathbf{x}_{k+1} = A_d \mathbf{x}_k + B_d u_k + \boldsymbol{\xi}_k + \mathbf{n}_k, \tag{9}$$

where $A_d = I + \Delta t\, A$, $B_d = \Delta t\, B$, $\boldsymbol{\xi}_k = \Delta t \boldsymbol{\xi}$, and $\mathbf{n}_k = \Delta t \mathbf{n}$ are obtained using forward-Euler discretization. This discrete-time formulation uses a sampling interval consistent with the resampled experimental data, enabling direct comparison of trajectories without additional interpolation.

In addition to the state process, sensory observations are modeled as:

$$\mathbf{y}_k = H \mathbf{x}_k + \boldsymbol{\omega}_k, \tag{10}$$

where $\boldsymbol{\omega}_k \sim \mathcal{N}(0, \Omega_\omega)$ is sensory noise. To account for sensory delay, the state is augmented to include past states, so that the observation matrix acts on the delayed state component.

3.3. Optimal feedback control

Building on the stochastic state-space formulation above, control is posed as a finite-horizon stochastic optimal feedback problem. Given an initial state $\mathbf{x}_0$ and horizon N, the controller minimizes

$$J = \mathbb{E}\left[\mathbf{x}_N^\mathsf{T} Q_N \mathbf{x}_N + \sum_{k=0}^{N-1}\left(\mathbf{x}_k^\mathsf{T} Q_k \mathbf{x}_k + u_k^\mathsf{T} R_k u_k\right)\right], \tag{11}$$

where $Q_k \succeq 0$ penalizes state deviations and $R_k > 0$ penalizes effort. In our implementation, $R_k = 1$ is constant, while Q_k is zero during the movement phase and becomes nonzero during the final stationary phase (last 50 time steps) to enforce stabilization of the cart and pendulum at the target. In particular, the state penalties are applied to the cart position and velocity and to the pendulum angle and angular velocity, whereas the reference states x_{ref} and $\dot{x}_{\text{ref}}$ evolve dynamically as part of the system and are not penalized.

The optimal feedback gains L_k and estimator gains K_k are computed iteratively using coupled optimal control and estimation recursions (Todorov, 2005). The resulting control law is

$$u_k = -L_k \hat{\mathbf{x}}_k, \tag{12}$$

where $\hat{\mathbf{x}}_k$ is the estimated state provided by the Kalman filter:

$$\hat{\mathbf{x}}_{k+1} = A_d \hat{\mathbf{x}}_k + B_d u_k + K_k(\mathbf{y}_k - H\hat{\mathbf{x}}_k) + \boldsymbol{\eta}_k, \tag{13}$$

where $\hat{\mathbf{x}}_k$ is the estimated state, K_k is the Kalman gain, and $\boldsymbol{\eta}_k \sim \mathcal{N}(0, \Omega_\eta)$ represents internal state estimation noise.

3.4. Internal models

The state equations (7) represent the full dynamics of the simulated task. The OFC controller, as described above, can be solved using an internal model that is simpler than the task model. In addition to the full-detail internal model, which parallels the task dynamics, we consider two simplified internal models.

No-impedance model. The first simplified internal model removes all states related to the arm impedance (x_{ref} and $\dot{x}_{\text{ref}}$) and the corresponding rows/columns in A, B, H. In this model, the muscle force is directly acting on the cart.

Rigid model. The second simplified model removes the coupling between the pendulum and the cart by setting $G = 0$. Therefore, starting with initial conditions $\phi = \dot{\phi} = 0$, the cart and pendulum will move together as a single rigid body.

4. Simulations and data analysis

For any of the three internal models (full-detail, no-impedance, rigid), we solved for OFC gains and applied the controller to the system with full task dynamics to simulate the task under the same settings as the experimental data (Bazzi et al., 2023). In the simulated task, the distance to the target was 0.25 m, and the movement duration was 1.5 s or 1.36 s, corresponding to the average trial time in experimental blocks 3 and 4, respectively. In both cases, the simulations continued for another 0.5 s in which the cart was held stationary at

the target. Since the simulations are stochastic, 10 simulations were run for each scenario, and the resulting trajectories were averaged across runs.

To analyze the results, experimental trajectories were aligned to movement onset, resampled to $\Delta t = 0.01$ s, and truncated to a common duration (average of the data), ensuring consistent time alignment without introducing temporal warping across trials and simulations. Full details about data processing are given in Appendix A.

After alignment, and for each experimental trial, we compared the kinematic trajectories $(x, \dot{x}, \phi, \dot{\phi})$ with the simulated ones. For each trajectory, the root-mean-squared error (RMSE) was computed per trial. For example, for comparing x in trial i:

$$\mathrm{RMSE}_i = \sqrt{\frac{1}{N}\sum_{k=1}^{N}\big(x_i(k) - x_{\mathrm{sim}}(k)\big)^2}, \tag{14}$$

and the population mean ± SD was reported. Additionally, normalized RMSE (nRMSE) was computed as a percentage of the range of the experimental trajectories to facilitate cross-variable comparison. These per-trial RMSE timelines served as the primary quantitative metric for evaluating model accuracy.

Following Bazzi et al. (2023), we also computed the ratio between the first and second positive peaks of the hand velocity $\dot{x}(t)$:

$$\text{Peak Ratio} = \frac{\dot{x}_{\mathrm{peak1}}}{\dot{x}_{\mathrm{peak2}}}. \tag{15}$$

Peaks are identified as local maxima in the velocity profile during the movement phase, and the first two positive peaks are used; values close to one indicate similar peak magnitudes, and larger values indicate attenuation of the second peak.

5. Results

5.1. Comparison OFC with experimental data

Figure 3 compares the predictions of the OFC (solved with the full-detail internal model) with experimental data for both a representative participant and the full participant population across Blocks 3 and 4. In Columns 1–2, the simulated mean closely tracks the experimental mean across all state variables, and the spread of stochastic simulations is comparable to the variability observed across trials. In Columns 3–4, the OFC mean remains within the distribution of participant means for all variables, indicating that the fixed-parameter model captures population-level behavior without participant-specific tuning. The main discrepancies occur in derivative signals: simulated peaks are slightly earlier and larger than the data.

The group-level comparisons in Columns 3–4 of Figure 3 further show that the OFC mean lies within the distribution of participant means for both blocks. The agreement is strongest for x and $\dot{\theta}$, while simulated θ and $\dot{x}$ show more pronounced peaks than the data. Quantitatively, the per-participant RMSE and nRMSE values in Figure 4 remain low and comparable to those of the representative subject, indicating that the fixed-parameter OFC model generalizes well across individuals and does not rely on idiosyncratic tuning.

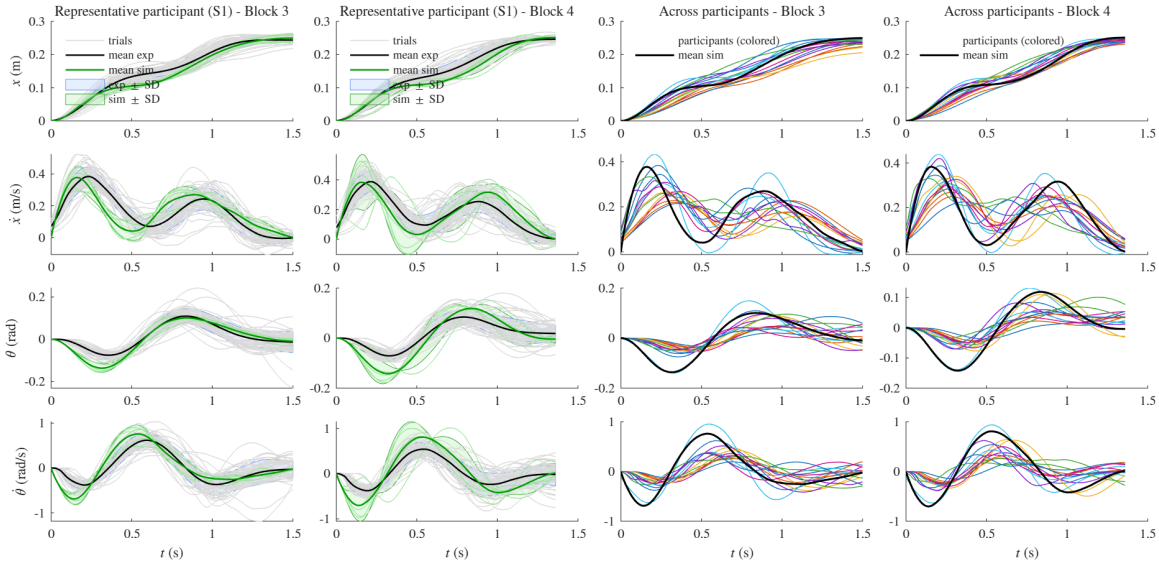

Figure 3: Comparison of OFC simulations with experimental data across the two task durations. Columns 1–2 show a representative participant (S1) for Blocks 3 and 4, respectively, including individual trials (gray), experimental mean (black), simulated rollouts (light green), and simulation mean (dark green), with shaded ±SD bands for experiment and simulation. Columns 3–4 show participant-mean trajectories (colored) for Blocks 3 and 4 together with the OFC mean (black).

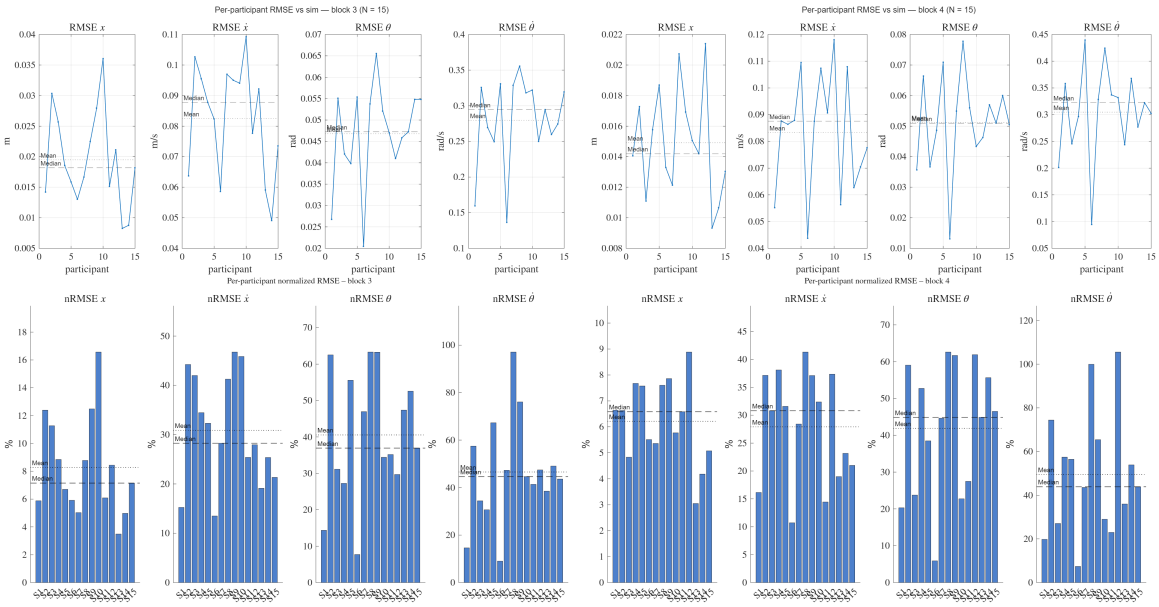

Figure 4: Per-participant error metrics across all states. **Top row:** RMSE for Block 3 (left) and Block 4 (right). **Bottom row:** nRMSE (%) for Block 3 (left) and Block 4 (right). Dotted and dashed lines indicate mean and median across participants.

5.2. Internal model variants

To examine the influence of internal model accuracy on control behavior, we simulated three OFC controllers, each solved using one of the three internal models (full-detail, rigid, and no-impedance), but all operating on the same true cart-and-pendulum (Figure 5). The full-detail internal model reproduced the characteristic double-peaked velocity structure

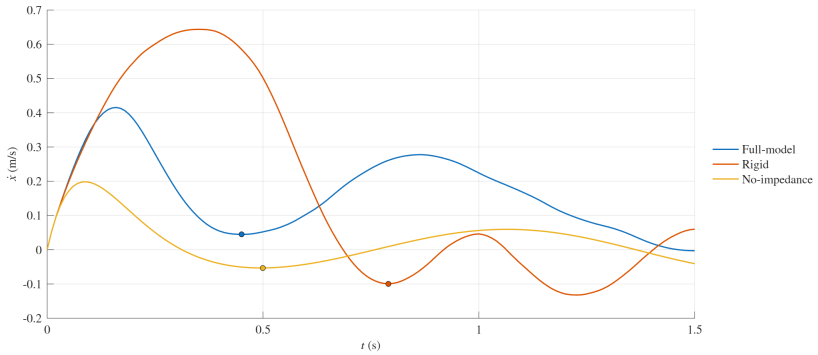

Figure 5: Cart velocity predicted by OFC controllers with different internal models. The true plant that is controlled is fixed, and the final time is 1.5 s.

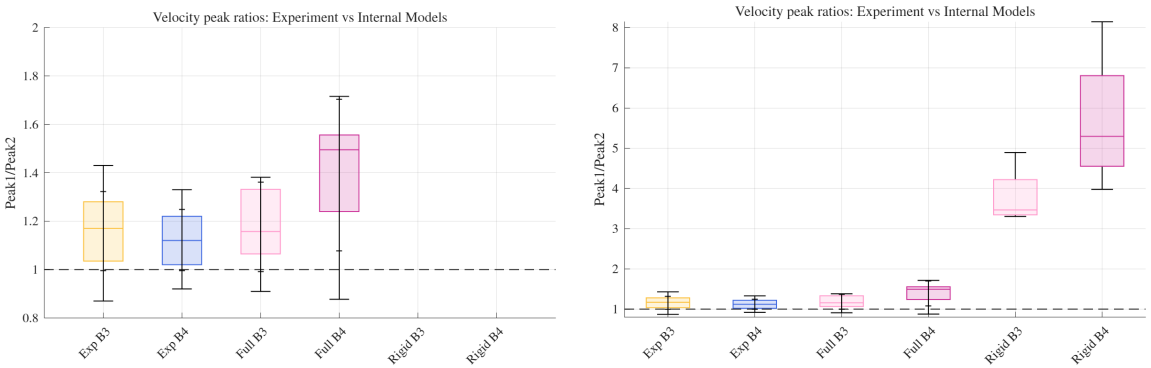

Figure 6: Peak1/Peak2 ratios for experiment and OFC internal models. Box plots show the distribution per condition across all trials (experiment) or simulations runs (OFC); the dashed line marks a ratio of 1 (equal peaks). The left and right panels show the same plots but with different axis scales (the left panel is zoomed in). Experimental Blocks 3 and 4 and the full-detail OFC exhibit similar ratios slightly above 1. Rigid and no-impedance internal models produce unrealistically large ratios (most values are off the scale in the left panel), indicating loss or severe attenuation of the second peak. The no-impedance results are not shown here because the second peak was absent.

observed experimentally (Figure 3). The rigid model failed at stabilizing the cart in time at the target, while the no-impedance model did not reach the target and exhibited reduced velocity amplitude and delayed peaks.

Following Bazzi et al. (2023), we also quantified the velocity profile using the ratio between the first and second positive peaks of cart velocity (peak1/peak2). Figure 6 summarizes this metric for experimental Blocks 3 and 4 in comparison with OFC simulations with the three internal models at the corresponding durations.

For experimental data, peak1/peak2 clustered around 1.1–1.2 in both blocks (peak1 usually larger than peak2). The full-detail OFC produced similar ratios in block 3, while slightly accentuating the first peak in block 4, resulting in a larger peak1/peak2 ratio but remaining within the experimental range. In contrast, the rigid and no-impedance internal models yielded extremely large ratios (off-scale in the zoomed-in right axis of Figure 6), reflecting a strongly diminished or effectively absent second peak. The no-impedance model is omitted from the plot, as it did not produce the characteristic two-peak velocity profile required to compute a meaningful Peak1/Peak2 ratio. These results indicate that, among the tested controllers, only the OFC with a physically faithful internal model reproduces the characteristic two-burst velocity pattern observed across participants.

6. Discussion

We examined whether an explicit stochastic OFC controller, defined on a biomechanically inspired cart-pendulum-impedance model, could account for key features of human performance in a complex object manipulation task. Using only fixed physical parameters and generic cost weights, the OFC simulations reproduced several hallmarks of the experimental behavior: smooth transport of the cart, underdamped yet stabilized internal oscillations, and a robust double-peaked velocity structure across movement durations. Quantitative errors between model predictions and human trajectories remained modest for both single-participant and group-level comparisons, suggesting that a principled optimal control formulation captures much of the structure of coordinated object control (Todorov and Jordan, 2002; Todorov, 2004; Franklin and Wolpert, 2011). While sensitivity to internal model mismatch is well established, our results show how these effects appear in a biologically relevant task and match human kinematics.

A central motivation for this work was the proposal by Bazzi et al. (2023) that humans may rely on *simplified* internal models for complex objects. Unlike Bazzi et al. (2023), which did not formulate the problem within a stochastic optimal feedback control framework—the leading theory in computational motor neuroscience—our approach explicitly integrates realistic internal dynamics into an OFC formulation and evaluates its ability to reproduce human behavior without parameter tuning. By explicitly manipulating the controller's internal dynamics while keeping the true plant fixed, we showed that these modeling choices have distinct kinematic signatures. When the controller possessed an accurate internal model with realistic coupling and impedance, the resulting velocity profiles and peak-velocity ratios overlapped the experimental distributions. In contrast, removing impedance or assuming a rigid (uncoupled) object in the internal model yielded exaggerated or qualitatively different velocity peak ratios and misaligned timing, inconsistent with the human data. Thus, within the OFC framework, realistic internal dynamics appear necessary to match the observed kinematic structure, placing constraints on which "simplified" models remain compatible with behavior. Although alternative cost structures or impedance tuning might partially compensate for simplified internal models, our results show that under a fixed and well-established cost formulation Todorov (2004); Scott (2004), mismatched dynamics lead to systematic deviations from experimentally observed behavior.

More broadly, our findings support the view that human manipulation of objects with internal dynamics can be understood as an optimal feedback control based on internal models that respect key mechanical features of the plant (Scott, 2004; Shadmehr and Krakauer, 2010; Wolpert et al., 2011). While humans may not implement the exact linear-quadratic-Gaussian solution used here, the success of this fixed-parameter OFC model—together with its failures under severely mismatched internal models—suggests that coupled dynamics and endpoint impedance play an important role in shaping behavior. This does not imply that the nervous system explicitly represents the full dynamics in this form, but rather that behavior is consistent with control policies that account for key physical features of the task. This is in line with prior work on dynamic primitives and coordination strategies in object manipulation (Hogan and Sternad, 2012) and suggests that "simplified" models used by the nervous system remain quantitatively faithful to the underlying physics. These findings also have implications for robotics and control, where handling objects with internal

dynamics remains challenging. Incorporating physically grounded internal models within optimal feedback controllers may improve robustness in such settings.

Finally, our analysis has limitations. We considered a linearized plant around small angles ($\phi \approx 0$), which is consistent with the experimental regime where oscillations remained bounded and stabilization was maintained throughout the movement. Under larger amplitudes, nonlinear effects would alter the coupling between cart and internal dynamics, potentially changing peak structure and timing. Thus, the present results should be interpreted as characterizing locally optimal feedback strategies near the stabilized operating region, rather than global behavior across all possible swing amplitudes. In addition, we assumed a restricted cost structure and Gaussian noise, and focused on a single cup-and-ball task with a pre-established internal model, whereas real neuromuscular systems involve nonlinearities, context-dependent objectives, and learning across tasks and over time(Lizarraga and Shadmehr, 2023; Diedrichsen and Shadmehr, 2023). Future work could incorporate richer objective functions, perturbation paradigms, and multi-segment limb dynamics to test how far OFC with structured internal models can scale. Nonetheless, by tightly coupling a mechanistic controller with population-level human data, this study provides a concrete step toward bridging normative optimal control theory and empirical motor behavior in complex object tasks.

References

Salah Bazzi, Stephan Stansfield, Neville Hogan, and Dagmar Sternad. Simplified internal models in human control of complex objects. *eLife*, 12:e81252, 2023.

Jörn Diedrichsen and Reza Shadmehr. Motor control, adaptation, and learning in humans. *Current Opinion in Neurobiology*, 83:102744, 2023.

David W Franklin and Daniel M Wolpert. Computational mechanisms of sensorimotor control. *Neuron*, 72(3):425–442, 2011.

Christopher M Harris and Daniel M Wolpert. Signal-dependent noise determines motor planning. *Nature*, 394(6695):780–784, 1998.

Neville Hogan and Dagmar Sternad. Dynamic primitives of motor behavior. *Biological Cybernetics*, 106(11–12):727–739, 2012.

Vincent S Huang, Adrian M Haith, Pietro Mazzoni, and John W Krakauer. Optimal control models of adaptive learning in the human motor system. *Progress in Brain Research*, 191: 39–60, 2011.

Timothy P Lillicrap and Stephen H Scott. Adaptive tuning of motor responses to environmental dynamics. *Frontiers in Computational Neuroscience*, 7:34, 2013.

Itziar Lizarraga and Reza Shadmehr. Computational principles of movement neuroscience. *Nature Reviews Neuroscience*, 24(1):46–61, 2023.

Stephen H Scott. Optimal feedback control and the neural basis of volitional motor control. *Nature Reviews Neuroscience*, 5(7):532–546, 2004.

Reza Shadmehr and John W Krakauer. Error correction, sensory prediction, and adaptation in motor control. *Annual Review of Neuroscience*, 33:89–108, 2010.

Reza Sharif Razavian, Mohsen Sadeghi, Salah Bazzi, Rashida Nayeem, and Dagmar Sternad. Body mechanics, optimality, and sensory feedback in the human control of complex objects. *¡update with final journal or preprint server¿*, 2023.

Emanuel Todorov. Optimality principles in sensorimotor control. *Nature Neuroscience*, 7 (9):907–915, 2004.

Emanuel Todorov. Stochastic optimal control and estimation methods adapted to the noise characteristics of the sensorimotor system. *Neural Computation*, 17(5):1084–1108, 2005.

Emanuel Todorov and Michael I Jordan. Optimal feedback control as a theory of motor coordination. *Nature Neuroscience*, 5(11):1226–1235, 2002.

Daniel M Wolpert, Jörn Diedrichsen, and J Randall Flanagan. Principles of sensorimotor learning. *Nature Reviews Neuroscience*, 12(12):739–751, 2011.

Appendix A. Data Processing and Alignment

To enable quantitative comparison between experimental trajectories and OFC simulations, all recorded data were processed using a standardized alignment pipeline.

A.1. Overview

Each experimental block contained multiple single-trial recordings of hand (cup) and object motion. Trials varied in onset time, duration, and oscillation pattern, requiring temporal normalization before averaging or comparison with simulated trajectories. Figure 7 shows the raw trajectories for two representative participants in Blocks 3 and 4, illustrating the trial-to-trial variability in both position and angular coordinates.

A.2. Preprocessing

Each trial was processed as follows: (1) time was zeroed so that t=0 corresponded to the first sample; (2) hand velocity $\dot{x}(t)$ was low-pass filtered at 8 Hz (2nd-order Butterworth, zero-phase), and movement onset was defined when the filtered speed exceeded $\max(0.02\ \text{m/s},\ 3\,\text{median}|\dot{x}|)$ for at least 80 ms; (3) trajectories were trimmed from onset and resampled at Δt=0.01 s using piecewise-cubic interpolation; and (4) the signals $x, \dot{x}, \phi, \dot{\phi}$ were truncated to the common minimum duration N_{common} shared by the experimental and simulated datasets.

A.3. Simulation horizon matching

Because participants' actual movement durations differed slightly from the instructed values, the OFC simulations used horizons of 1.50 s (Block 3) and 1.36 s (Block 4), matching the empirical mean durations rather than the nominal 1.40 s and 1.20 s. This ensured consistent temporal alignment between experimental and simulated trajectories without any artificial curve shifting.

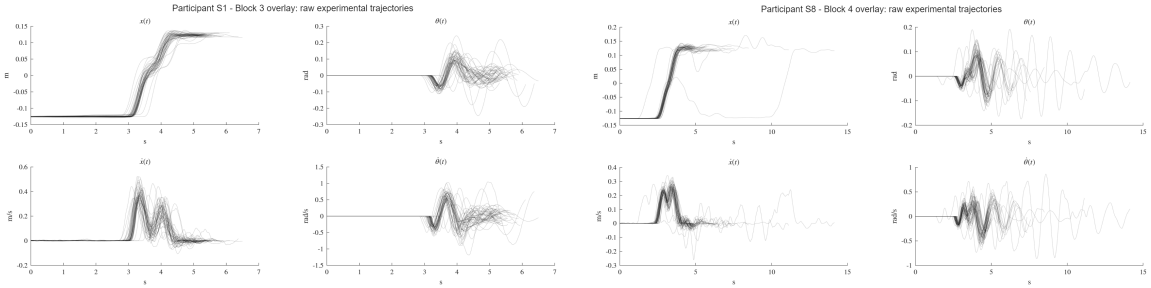

Figure 7: Raw experimental trajectories from Two representative participant. Each gray line shows one trial. Trials display variability in onset, duration, and oscillation amplitude, motivating the preprocessing and alignment steps described in Section 4.